Research Article

Interfacial structure between TiN sintered ceramics with and without an Fe-containing grain boundary phase and Ag–Cu eutectic brazing filler material

Nobuyuki Terasaki[1,3] · Naochika Kon[2] · Hajime Chiba[2] · Touyou Ohashi[1] · Tohru Sekino[3]

© The Author(s) 2022   OPEN

Abstract

To focus on the interfacial reaction between the Ag–Cu alloy layer and TiN in active metal brazing, the Ag–Cu brazed interfacial structures between Cu and two types of TiN sintered ceramics fabricated by different methods were examined. No grain boundary phase components consisting of the Ni-containing Fe phase or Mo_2C were detected on the TiN grain surfaces of the TiN liquid-phase sintered ceramic bonding surfaces before brazing. The brazed specimens were heated at 850 °C for 0.5 h. No Cu/TiN solid-phase sintered ceramic bonding was obtained. The Ag–Cu alloy layer was bonded onto the TiN grains in the TiN liquid-phase sintered ceramic through an Fe- and Ni-containing segregation layer. This segregation layer was formed by an interfacial reaction between the TiN grains and the Ni-containing Fe in the TiN liquid-phase sintered ceramic dissolved in the Ag–Cu liquid phase.

1 Introduction

To realize a carbon-free society in which the effects of global warming can be suppressed, many countries have been actively developing ways to improve energy efficiency and utilize renewable energy sources. Renewable energy sources such as solar and wind energy that do not emit carbon dioxide as a greenhouse gas are considered important for a future carbon-free society and can be easily connected to the grid through high-voltage direct current (HVDC) transmission [1–5]. HVDC transmission is characterized by higher transmission efficiency than conventional alternating current (AC) transmission. A copper (Cu)–aluminum nitride (AlN) substrate, in which Cu is bonded onto an AlN substrate with low electrical conductivity and high thermal conductivity, is suitable for the

AC/DC conversion modules that are needed to connect HVDC technology to the consumer AC power grid. The power modules used in HVDC transmission systems consist of high-voltage, large-capacity power semiconductor chips such as silicon (Si) insulated gate bipolar transistors (IGBTs) and silicon carbide (SiC) metal–oxide–semiconductor field-effect transistors (MOSFETs).

Both the direct copper bonding method [6–8] and the active metal bonding (AMB) method [9–13] have been used industrially for bonding between Cu and AlN. Above all, AlN–AMB substrates manufactured by the AMB method have been widely used for high-voltage applications such as HVDC and electric railways [1–5, 14]. The AMB method is a bonding technique that uses a Ag–Cu eutectic-based brazing material and active metals with a high reactivity to promote an interfacial reaction with inert ceramic surfaces

such as Ti, Zr, and Hf [9–13, 15–20]. The Cu/AlN bonding interfacial structure is characterized by a Ag–Cu alloy layer consisting of both a Ag-rich phase (a solid solution of Cu in Ag) and a Cu-rich phase (a solid solution of Ag in Cu), and a titanium nitride (TiN) layer formed by the interfacial reaction between Ti and AlN when using a Ag–Cu–Ti brazing alloy [9–13]. Most importantly, according to our previous work, a TiN layer is always continuously formed at the Cu/AlN interface to achieve highly reliable Cu/AlN bonding [11]. This implies that two types of interfacial reactions proceed in the AMB method: (i) a TiN layer formation reaction; and (ii) an interface formation reaction between the Ag–Cu layer and TiN layer.

In the internal structure of the TiN layer, Cu and Ag inclusions derived from the Ag–Cu based brazing material have been detected at the Cu/AlN part of the substrate/braze interface in work on the wettability of AlN-based ceramics using Ag–Cu–Ti AMB alloys by Taranets et al. [11], in work on the heat transfer characteristics of active brazed ceramic–metal joints by Sivaprahasam et al. [12], and in a model of interfacial evolution for a Cu-metalized polycrystalline AlN substrate using Ag–Ti paste by Zhang et al. [13]. In addition, our recent work has clearly shown that the TiN layer formed by the interfacial reaction between the Ag–Cu–Ti brazing filler and AlN is a composite of TiN grains and a grain boundary phase consisting of Ag and Cu [21]. In the present work, to focus on the interfacial reactions between the Ag–Cu alloy and TiN grains, we investigated in detail the interfacial structures between the Cu(Ag)-rich phase and TiN grains formed by Ag–Cu brazing of Cu plates on TiN sintered ceramics that contained no Cu and Ag inclusions and were fabricated by a solid/liquid-phase sintering method.

2 Experimental method

In this work, two different sintering methods were selected to produce the TiN layer. One was a commercial TiN solid-phase sintered ceramic (diameter 50.8 mm × 6 mm) fabricated by the solid-phase sintering method, in which there was no grain boundary phase composed of metal components, and this was cut into a 10 mm × 10 mm × 6 mm rectangular parallelepiped. The other was TiN–8.4 wt% Fe–2.2 wt% Ni–1.1 wt% C–3.8 wt% Mo_2C, which was fabricated by the liquid-phase sintering method (referred to as the TiN liquid-phase sintered ceramic). TiN ($D_{50} = 1.3$ μm), Fe

($D_{50} = 6.1$ μm), Ni ($D_{50} = 2.5$ μm), C ($D_{50} = 4.7$ μm), and Mo_2C ($D_{50} = 1.8$ μm) powders were added to ethanol and mixed for 40 h in a ball mill together with tungsten carbide balls (3 mm diameter). D_{50} is the 50th percentile of volume-based grain size. The resulting mixture was dried at 150 °C for 3 h under vacuum, and then formed into a cylinder (diameter 20 mm × 8 mm) at a pressure of 200 MPa. The molding was sintered at 1400 °C for 2 h in N_2 containing 3 vol% H_2 at atmospheric pressure and then formed into a 10 mm × 10 mm × 6 mm rectangular parallelepiped by grinding. The relative densities of these solid- and liquid-phase sintered ceramics were 81.9% and 99.8%, respectively, indicating that the TiN liquid-phase sintered ceramics were sufficiently densified. In addition, the area ratio of TiN grains to the grain boundary phase on the surface to be bonded to the TiN liquid-phase sintered ceramic is about 80:20. The concentrations of impurities in the TiN solid-phase sintered ceramic as found by inductively coupled plasma optical emission spectrometry (ICP-OES) are shown as Table 1. The TiN solid-phase sintered ceramic had purity of > 99.9 wt%. Of the nine impurities including Al, K, and Ca, the largest impurity concentration was Fe (0.018 wt%). These impurities would be derived from the TiN grains used as a raw material for the TiN solid-phase sintered ceramic, or from the Ti material used as a raw material for the TiN grains. In addition, this Fe impurity concentration is about 0.2% of the Fe concentration in the TiN liquid-phase sintered ceramic. Furthermore, an 800-μm-thick oxygen-free copper (OFC) plate and a 50-μm-thick Ag–Cu eutectic brazing foil (Ag–28 wt%Cu; eutectic temperature: 780 °C) [22] were selected as the materials to bond onto the TiN sintered ceramic to reproduce the same interfacial structure as the Cu–bonded nitride ceramic fabricated by the AMB method. These materials were cut into 10 mm × 10 mm squares and then layered in the following order: Cu, Ag–Cu eutectic brazing foil, TiN solid- or liquid-phase sintered ceramic, Ag–Cu eutectic brazing foil, Cu. The layered specimens were heated under vacuum at 850 °C for 0.5 h under a compressive stress of 1 MPa, with heating and cooling rates of 10 °C/min.

The surface and cross-section of the TiN sintered ceramic were observed by scanning electron microscopy (SEM) and auger electron spectroscopy (AES). AES analysis and SEM observation of the TiN sintered ceramic surface were performed using a PHI 700 system (ULVAC-PHI, Inc.) operated at 10 kV. For cross-sectional SEM analysis of the

Table 1 Concentrations of impurities related to the TiN solid-phase sintered ceramic by ICP-OES

Concentration/wt%								
Al	K	Ca	Cr	Mn	Fe	Co	Nb	Mo
0.012	0.015	0.002	0.002	0.005	0.018	0.010	0.002	0.003

TiN sintered ceramic, metallography specimens mounted in an acrylic polymer at room temperature were polished using standard metallographic techniques, with final polishing performed using an argon-based ion beam polisher (ArBlade 5000, Hitachi High-Tech). The microstructures of all cross-sectional specimens were observed using a GeminiSEM 500 system (Carl Zeiss AG) operated at 1.8 kV. In addition, cross-sections of Cu/TiN sintered ceramic/Cu brazed specimens, which were prepared in the same way as the TiN sintered ceramic cross-sectional specimens, were observed by SEM before more detailed observations were undertaken by scanning transmission electron microscopy (STEM). SEM observation and elemental analysis of the cross-sections were performed using the GeminiSEM 500 system with an energy-dispersive X-ray spectroscopy (EDS) system (NORAN System7, Thermo Fisher Scientific), which was operated at 1.8 kV and 7 kV. Cu/TiN thin sections for STEM analysis were prepared using a focused ion beam (FIB) system (Scios, Thermo Fisher Scientific), and their thickness was adjusted between 30 and 100 nm. The elemental distributions of the thin sections were evaluated using a Titan G2 ChemiSTEM system (Thermo Fisher Scientific) equipped with an EDS system (NSS7, Thermo Fisher Scientific) operated at 200 kV.

3 Results and discussion

Cross-sectional secondary electron (SE) images of the near surface of the TiN solid-phase sintered ceramic and the TiN liquid-phase sintered ceramic before brazing are shown in Fig. 1. It can be seen that the TiN solid-phase sintered ceramic contained a large number of voids. This was due to the low sinterability of TiN grains [23]. In contrast, the TiN liquid-phase sintered ceramic had a dense structure due to the bonding of the TiN grains through the crystalline grain boundary phase consisting of a Ni-containing Fe phase (Fe–44at%Ni, cubic, $Fm\bar{3}m$, $a = 3.586$ Å) [24–26] and Mo_2C (hexagonal, $P6_3/mmc$, $a = 2.994$ Å, $c = 4.732$ Å) [27]. In addition, it can be seen that although the surface of the TiN liquid-phase sintered ceramic finished by grinding had some fine cracks, it was flatter than the TiN solid-phase sintered ceramic. Surface SE images of the TiN solid-phase sintered ceramic and the TiN liquid-phase sintered ceramic before brazing, together with the AES spectra obtained from these surfaces are shown in Fig. 2. Some voids were present on the surface of the TiN solid-phase sintered ceramic and appeared to be connected to the voids inside the ceramic as shown in Fig. 1a. In addition, the shape of the AES spectra suggests that the impurities shown in Table 1 were not significantly segregated on the TiN grain surface (#1). In contrast, the SE image of
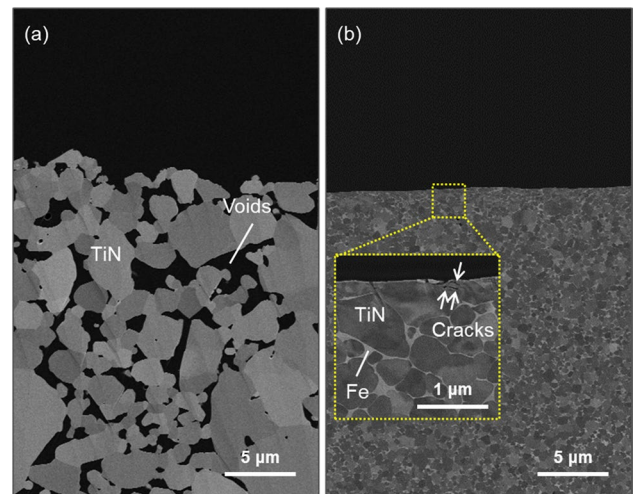

Fig. 1 Cross-sectional SE images of **a** the TiN solid-phase sintered ceramic and **b** the TiN liquid-phase sintered ceramic near the surface
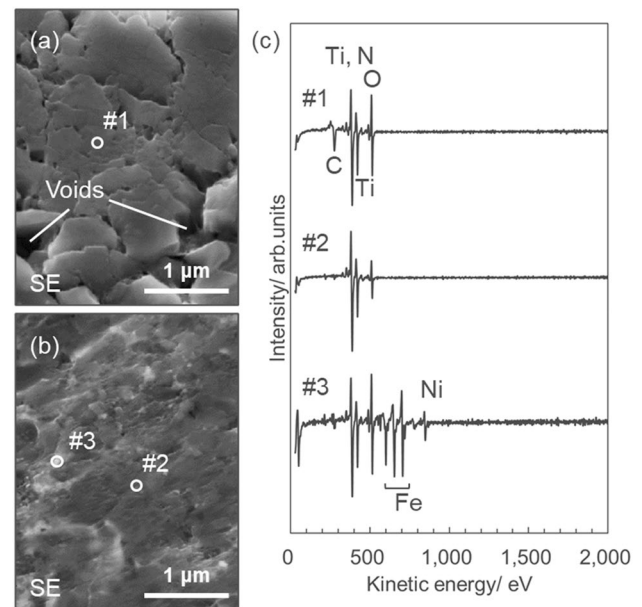

Fig. 2 Surface SE images of **a** the TiN solid-phase sintered ceramic and **b** the TiN liquid-phase sintered ceramic. **c** AES spectrum obtained from areas marked by white open circles in (**a**) and (**b**)

the TiN liquid-phase sintered ceramic is composed of different brightness regions (Fig. 1b). In the AES spectrum, the dark contrast region (#2) appears to be composed of the TiN phase with C and O, while the bright contrast region (#3) appears to be composed of the Ni-containing Fe phase in addition to the same TiN phase. Thus, no grain boundary phase components were present on the surface of the TiN grains on the surface to be bonded to the TiN liquid-phase sintered ceramics.

The appearance of the TiN solid-phase sintered ceramic and that of the Cu plates brazed with Ag–Cu eutectic brazing foil at 850 °C for 0.5 h are shown in Fig. 3. Poor adhesion can be seen between the Ag–Cu alloy layer and the TiN grains. This result is different from the bonding state

Fig. 3 Appearance of the TiN solid-phase sintered ceramic and Cu plates brazed with a Ag–Cu eutectic brazing foil after heating at 850 °C for 0.5 h

at the Ag–Cu alloy layer/TiN layer interface involving the interfacial reaction between the Ag–Cu–Ti liquid phase and the AlN substrate in the AMB method. In addition, Ag–Cu alloy layers were formed on the entire bonding surface of the copper plate and on the edge of its non-bonding surface. This suggests that a sufficient amount of Ag–Cu liquid phase generated during heating did not penetrate into the voids leading from the surface to interior of the TiN solid-phase sintered ceramic shown in Figs. 1a and 2a. Thus, good bonding was not achieved between the Ag–Cu alloy layer and the TiN grains by mechanical bonding, such as the anchor effect [28].

The cross-sectional energy-selective backscattered electron (EsB) image of the interface between the Cu and the TiN liquid-phase sintered ceramic after bonding for 0.5 h at 850 °C, together with the elemental distributions, is shown in Fig. 4. In contrast to the bonding state between Cu and the TiN solid-phase sintered ceramic shown in Fig. 3, here the Cu/TiN liquid-phase sintered ceramic brazing interface appears to fit the shape of the ceramic without any macroscopic gaps or pores. The most significant feature of the cross-sectional microstructure of the Cu/TiN liquid-phase
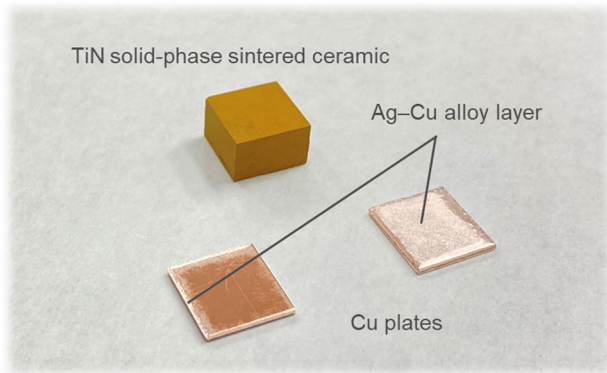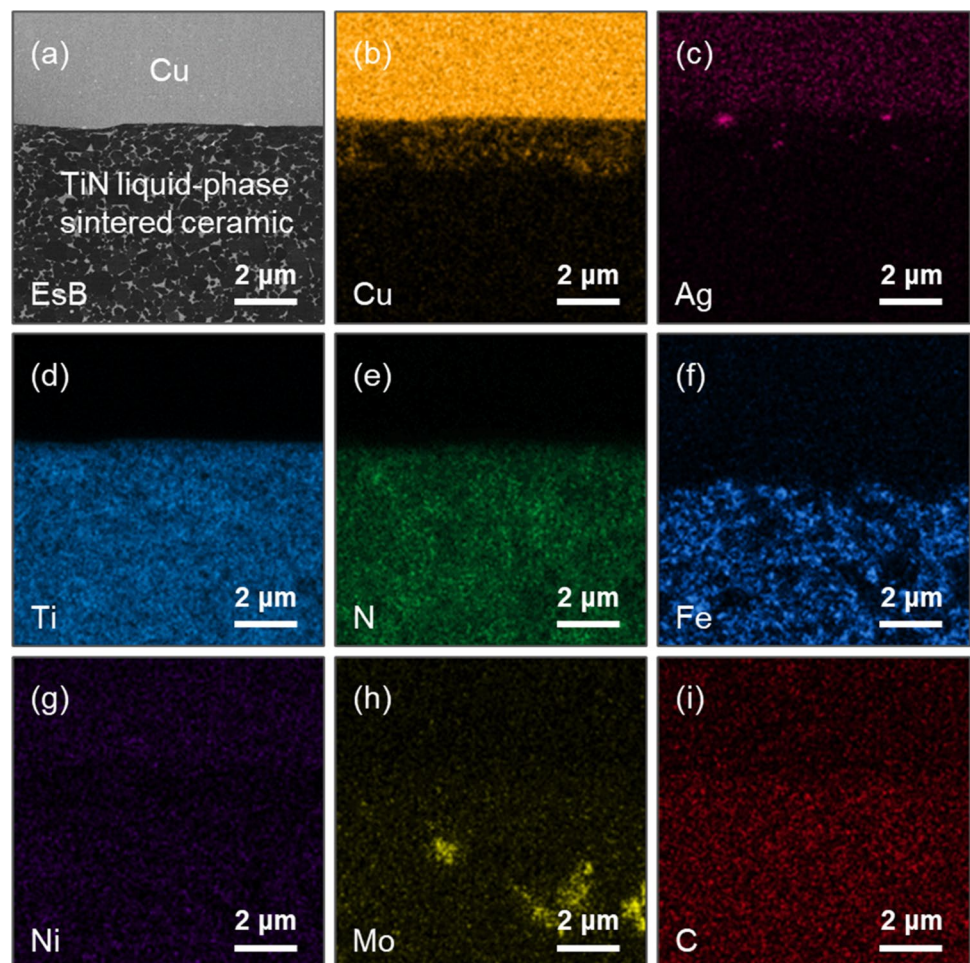

Fig. 4 **a** Cross-sectional EsB image of the Cu/TiN liquid-phase sintered ceramic interface after bonding for 0.5 h at 850 °C. **b**–**i** Elemental distributions of **b** Cu, **c** Ag, **d** Ti, **e** N, **f** Fe, **g** Ni, **h** Mo, and **i** C obtained by EDS

sintered ceramic is that the Ni-containing Fe phase was substituted for the Cu-rich and Ag-rich phases from the Cu/TiN liquid-phase sintered ceramic brazing interface to the interior of the TiN liquid-phase sintered ceramic to a depth of about 2 μm. This suggests that interdiffusion of the Ni-containing Fe phase with Cu(Ag)-rich phase could replace these phases while maintaining the shape near the brazed surface of the TiN liquid-phase sintered ceramics. In addition, no distinct signals of Fe and Ni can be seen in the Ag–Cu alloy layer, suggesting that the concentrations of these elements are below the limit of detection due to their diffusion to the Cu surface side. The Cu/TiN liquid-phase sintered ceramic macroscopic interfacial structures can be divided into three interfaces. The first is the Ag–Cu alloy layer/TiN brazing interface formed by the interfacial reaction between the Ag–Cu liquid phase and the TiN grains (Interface I). The second is the substituted Ag–Cu phase/TiN interface, where the grain boundary phases of the TiN liquid-phase sintered ceramic are substituted for the Ag–Cu brazing filler components (Interface II). The third is the interface between the TiN grains and the grain boundary phase without substitution by the Cu-rich and Ag-rich phases in the TiN liquid-phase sintered ceramic (Interface III).

A high-angle annular dark field (HAADF) image and elemental distributions of Interface I after brazing for 0.5 h at 850 °C are shown in Figs. 5 and 6 for the Cu-rich phase/TiN grain interface and the Ag-rich phase/TiN grain interface, respectively. The highest signal in the Fe and Ni maps is located uniformly at Interface I between the Cu-rich phase and TiN grain (Fig. 5f and g). By comparison, a Cu signal is detected at Interface I between the Ag-rich phase and TiN grain in addition to the Fe and Ni signals (Fig. 6b, f, and g). Cu segregates with Fe and Ni at Interface I between the Ag-rich phase and TiN grain, while the regions where these elements do not segregate correspond to very small voids of size 1 to 2 nm. Line EDS profiles of Interface I after brazing for 0.5 h at 850 °C are shown in Figs. 5j and 6j, where the line EDS profiles correspond to the white dashed arrows in Figs. 5b and 6b, respectively. The peak positions of the Fe and Ni signals at the interface between the Cu-rich phase and TiN grain almost overlap, as shown in Fig. 5j. The overlap of the peak positions between these elements is also detected at Interface I between the Ag-rich phase and TiN grain (Fig. 6j), while the peak position of the Cu signal is shifted toward the Ag-rich phase with respect to the peak positions of the Fe and Ni signals. No Fe or Ni was present on the TiN grain surface of the TiN liquid-phase sintered ceramic before brazing (#2 in Fig. 2c). These results suggest that the segregation layers containing Fe and Ni, which are expected to be austenite with Ni solid solution [25, 26], are formed by the interfacial reaction
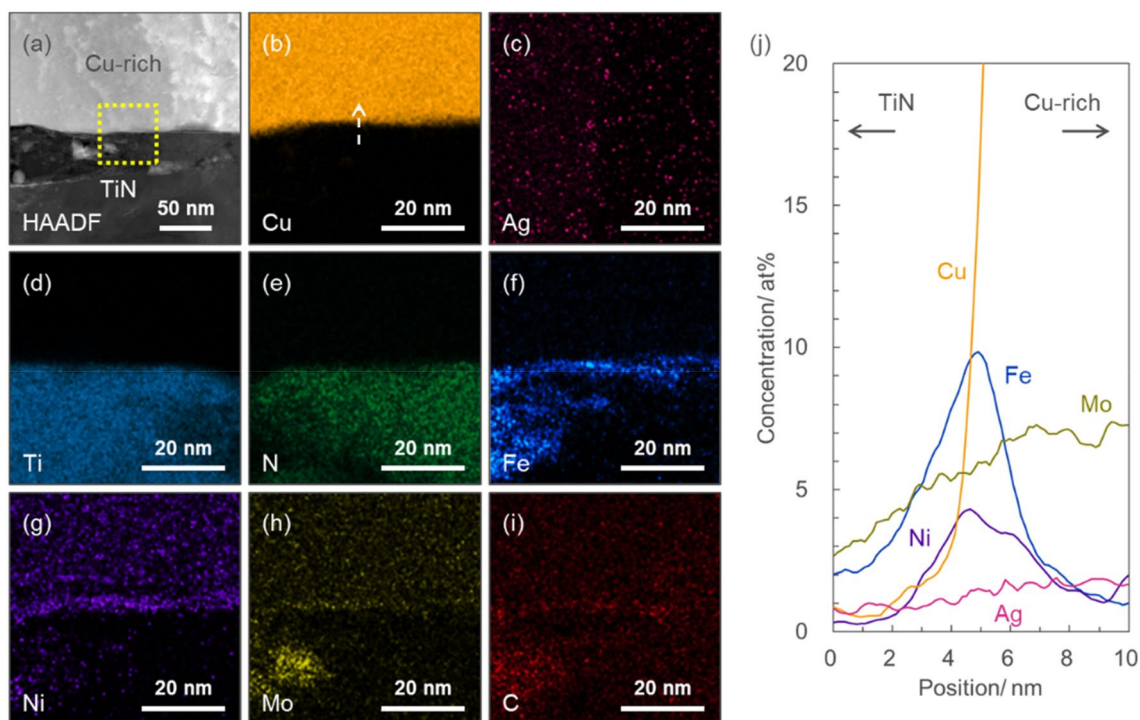

Fig. 5 **a** Cross-sectional HAADF image of the Cu-rich phase/TiN grain interface after brazing for 0.5 h at 850 °C. **b–i** Elemental distributions of **b** Cu, **c** Ag, **d** Ti, **e** N, **f** Fe, **g** Ni, **h** Mo, and **i** C obtained from the selected area marked in (**a**) by EDS. **j** Line EDS profile obtained along the white dashed arrow shown in (**b**)
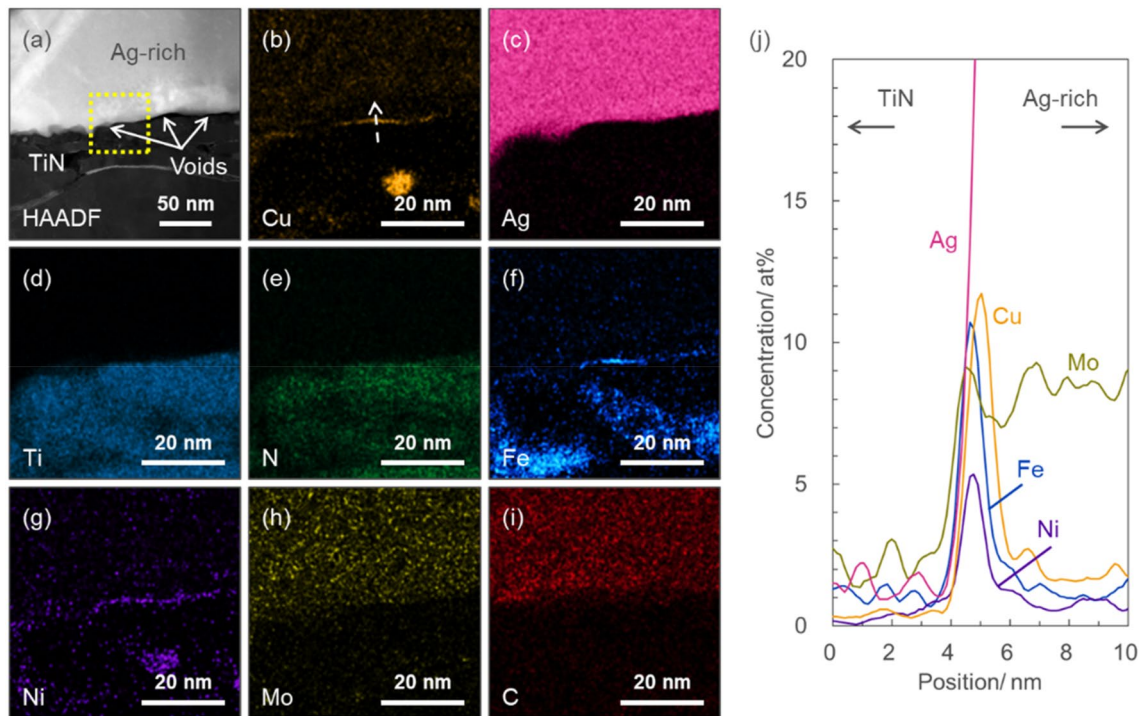
Fig. 6 **a** Cross-sectional HAADF image of the Ag-rich phase/TiN grain interface after brazing for 0.5 h at 850 °C. **b–i** Elemental distributions of **b** Cu, **c** Ag, **d** Ti, **e** N, **f** Fe, **g** Ni, **h** Mo, and **i** C obtained from the selected area marked in (**a**) by EDS. **j** Line EDS profile obtained along the white dashed arrow shown in (**b**)

between the TiN grains and the Ag–Cu liquid phase, which contained Fe and Ni components derived from the grain boundary phase of the TiN liquid-phase sintered ceramic. This means that both the Cu-rich and Ag-rich phases are not directly bonded to the TiN grain. On the other hand, such interfacial reactions seemed not to occur during brazing in the TiN solid-sintered ceramic system because the dissolution of TiN grains into the Ag–Cu liquid phase did not provide enough Fe, one of the impurities shown in Table 1. In addition, there appeared to be a Cu-containing segregation layer between the Ag-rich phase and the Fe- and Ni-containing segregation layer at Interface I between the Ag-rich phase and TiN grain.

A HAADF image and elemental distributions of Interface II after brazing for 0.5 h at 850 °C are shown in Figs. 7 and 8 for the substituted Cu-rich phase/TiN grain interface and the substituted Ag-rich phase/TiN grain interface, respectively. The highest signal in the Fe and Ni maps is located uniformly between the Cu-rich and Ag-rich phases and the TiN grain at Interface II, similar to Interface I (Figs. 5 and 6), as shown in Figs. 7f, g and 8f, g. In addition, a Cu signal was detected at Interface II between the substituted Ag-rich phase and TiN grain in addition to the Fe and Ni signals (Figs. 8b, f, and g). The line EDS profiles of Interface II in Figs. 7j and 8j, corresponding to the white dashed arrows in Figs. 7b and 8b, show that the Fe and Ni peak positions

coincided with the Cu-rich phase/TiN grain interface. In addition, the Cu peak position was shifted toward the Ag-rich phase compared with the Fe and Ni peak positions coinciding with the Ag-rich phase/TiN grain interface. Most importantly, these features of Interface II formed by interdiffusion between the grain boundary phase and the Ag–Cu liquid phase are in perfect agreement with those of Interface I formed by the interfacial reaction during brazing. Specifically, the interfacial structure across the Fe- and Ni-containing segregation layer is a feature common to the Cu-rich phase/TiN grain interface and the Ag-rich phase/TiN grain interface. Also, a Cu-containing segregation layer may have been present between the Ag-rich phase and Fe- and Ni-containing segregation layer at the Cu-rich/TiN grain interface for Interfaces I and II.

A HAADF image, elemental distributions, and a line EDS profile of Interface III (Mo_2C/TiN grain) after brazing for 0.5 h at 850 °C are shown in Fig. 9. The elemental distributions and line EDS profile are obtained from the selected area shown in Fig. 9a and the white dashed arrow shown in Fig. 9b, respectively. The highest uniform signal in the Fe map can be clearly seen at Interface III as shown in Fig. 9f. In addition, the Ni concentration of 6.2 at% at the Ni peak position is close to the value of about 4.9 at% in Mo_2C, which may appear unclear. However, the Ni peak position is consistent with the Fe peak position in the line
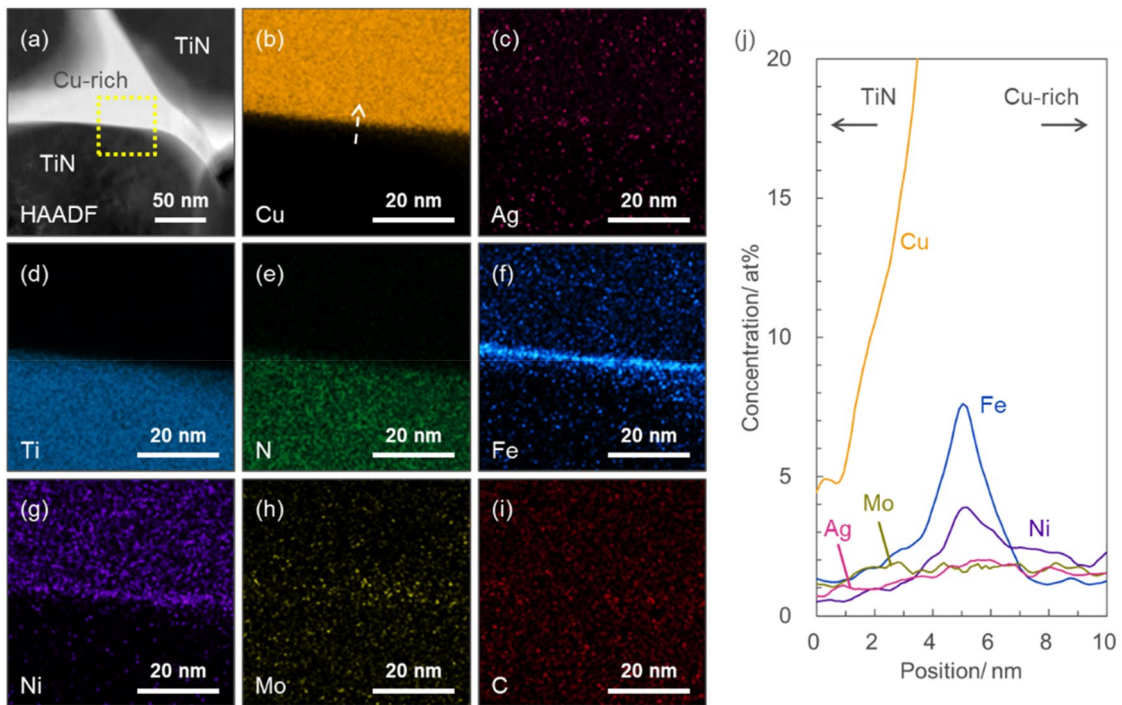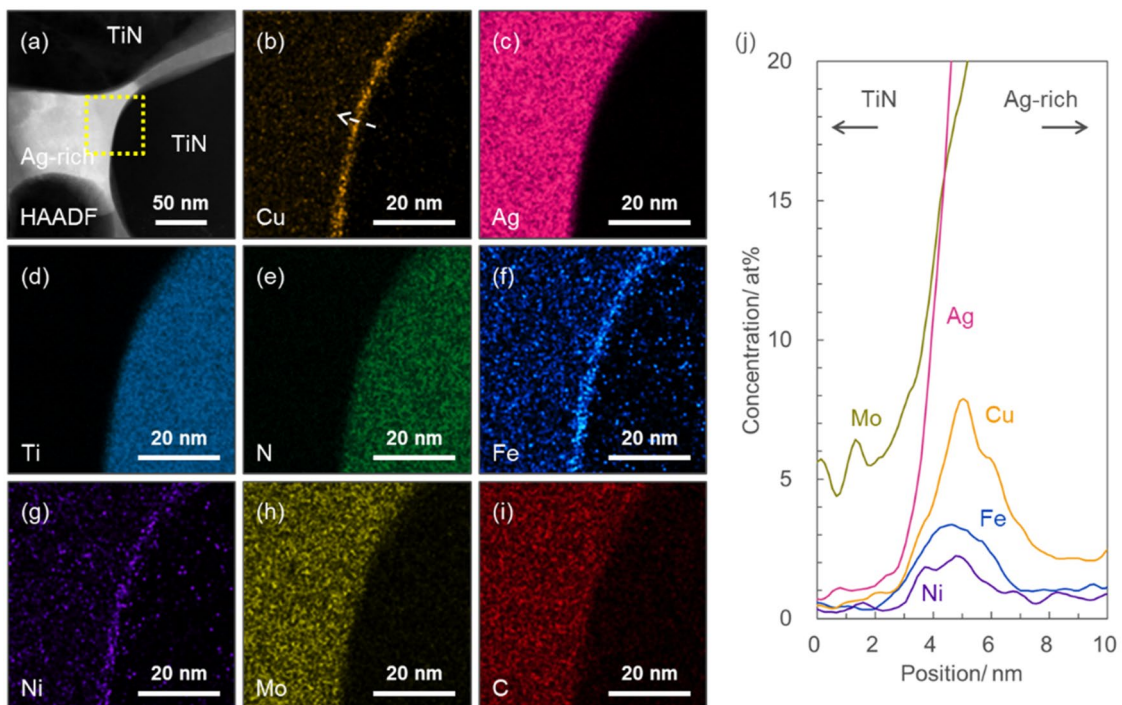
Fig. 7 **a** Cross-sectional HAADF image of the substituted Cu-rich phase/TiN grain interface after brazing for 0.5 h at 850 °C. **b–i** Elemental distributions of **b** Cu, **c** Ag, **d** Ti, **e** N, **f** Fe, **g** Ni, **h** Mo, and **i** C obtained from the selected area marked in (**a**) by EDS. **j** Line EDS profile obtained along the white dashed arrow shown in (**b**)
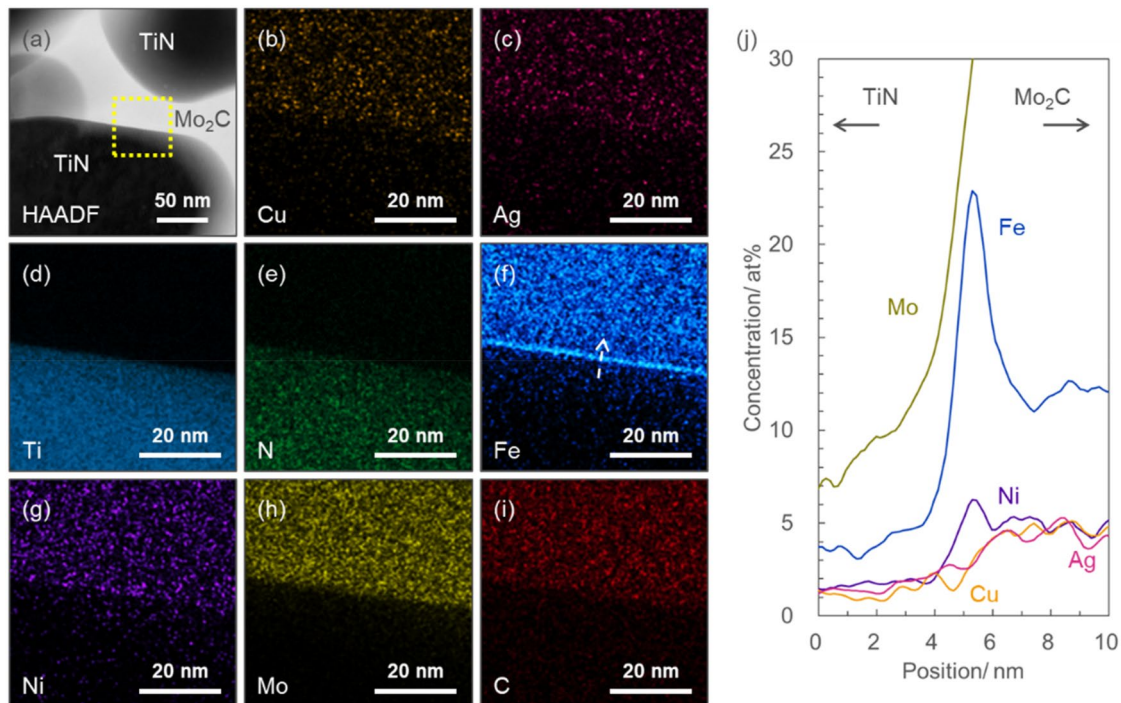

Fig. 8 **a** Cross-sectional HAADF image of the substituted Cu-rich phase/TiN grain interface after brazing for 0.5 h at 850 °C. **b–i** Elemental distributions of **b** Cu, **c** Ag, **d** Ti, **e** N, **f** Fe, **g** Ni, **h** Mo, and **i** C obtained from the selected area marked in (**a**) by EDS. **j** Line EDS profile obtained along the white dashed arrow shown in (**b**)

Fig. 9 **a** Cross-sectional HAADF image of the Mo$_2$C/TiN grain interface after brazing for 0.5 h at 850 °C. **b**–**i** Elemental distributions of **b** Cu, **c** Ag, **d** Ti, **e** N, **f** Fe, **g** Ni, **h** Mo, and **i** C obtained from the selected area marked in (**a**) by EDS. **j** Line EDS profile obtained along the white dashed arrow shown in (**f**)

EDS profile in Fig. 9j. It is suggested that the surfaces of TiN grains constituting the TiN liquid-phase sintered ceramic are covered by an Fe- and Ni-containing layer due to an interfacial reaction during the liquid-phase sintering process above the Ag–Cu brazing temperature. This means that the TiN grains are bonded to the grain boundary phase through the Fe- and Ni-containing segregation layer in the TiN liquid-phase sintered ceramic used in this work.

Combining the results of brazing between the Ag–Cu brazing filler metal and the TiN solid-phase sintered ceramic and those of the three sets of interfacial structures for the Cu brazed TiN liquid-phase sintered ceramic, a bonding mechanism for TiN grains to Cu-rich and Ag-rich phases is proposed, as illustrated in Fig. 10. During the liquid-phase sintering process (1400 °C), which is the manufacturing process for the TiN liquid-phase sintered ceramic, the surfaces of TiN grains are covered with an Fe- and Ni-containing segregation layer due to the interfacial reaction between the TiN grains and the grain boundary components consisting mainly of Fe. The TiN liquid-phase sintered ceramic used in this work is formed by the bonding of TiN grains with a grain boundary phase such as the Ni-containing Fe phase and Mo$_2$C through this Fe- and Ni-containing segregation layer. The surface to be bonded to the TiN liquid-phase sintered ceramic consists of flat TiN grains and a grain boundary phase due to the grinding process, as shown in Fig. 10a.

Therefore, no Fe- and Ni-containing segregation layer is present on the surfaces of the TiN liquid-phase sintered ceramics to be bonded. As shown schematically in Fig. 10b, the grain boundary components of the TiN liquid-phase sintered ceramic first dissolve into the Ag–Cu liquid phase above the Ag–Cu eutectic temperature, causing erosion of its grain boundary phases. Then, as this erosion progresses, the concentrations of Fe and Ni in the Ag–Cu liquid phase increase, promoting the interfacial reaction with TiN grains to form the Fe- and Ni-containing segregation layer on the surface of TiN grain, as shown in Fig. 10c. While this interfacial reaction is occurring, interdiffusion occurs between the grain boundary phase and the Ag–Cu liquid phase. After brazing, the Ag–Cu liquid phase separates into the Cu-rich and Ag-rich phases by solidification. Most importantly, the following interfacial structure is formed through this Fe- and Ni-containing layer: Cu-rich phase/Fe- and Ni-containing segregation layer/TiN grain and Ag-rich phase/ Cu-containing segregation layer/Fe- and Ni-containing segregation layer/TiN grain (Fig. 10d and e respectively). This suggests that the Fe- and Ni-containing segregation layer contributes to lowering the energy of the entire interfacial reaction system, and furthermore that formation of the Cu-containing segregation layer between the Ag-rich phase and the Fe- and Ni-containing segregation layer promotes stabilization of the interfacial structure. This implies that a
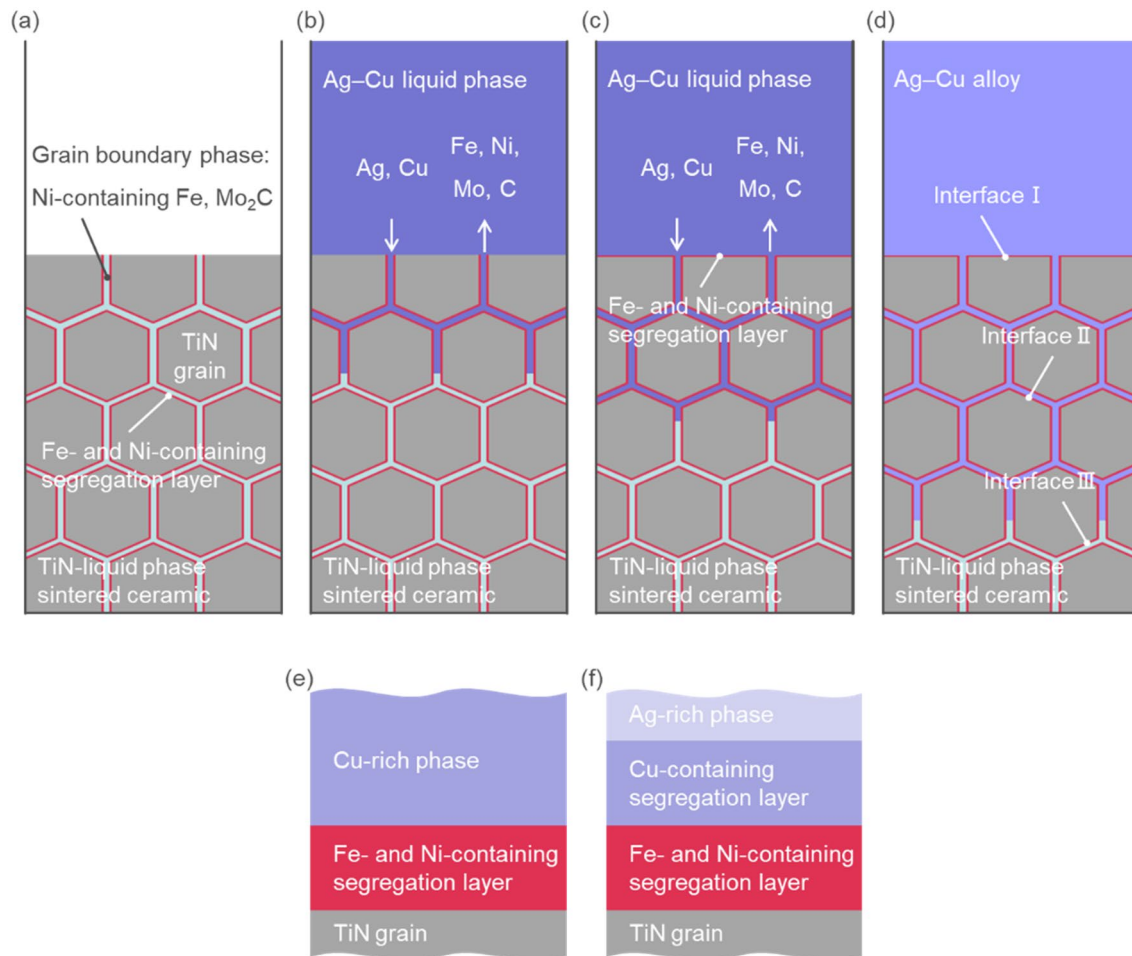
Fig. 10 a–d Schematic mechanism for the interfacial reaction between the TiN liquid-phase sintered ceramic and Ag–Cu eutectic brazing filler metal while heating above the Ag–Cu eutectic tem-perature. (**d**), **e** Details of the interfacial structures at (**e**) the Cu-rich phase/TiN grain interface and **f** the Ag-rich phase/TiN grain interface for Interface I and Interface II after heating

Cu-containing segregation layer may have been present between the Ag-rich phase and the Fe- and Ni-containing segregation layer. Taken together with the results of Ag–Cu brazing of the Cu plate onto the TiN solid-phase sintered ceramic, in which there was no grain boundary phase composed of metal components, the addition of elements to the interfacial reaction system capable of forming a segregation layer between the metal phase and the TiN grain is a key for achieving Ag–Cu brazing onto TiN grains.

4 Conclusions

In this work, the Ag–Cu brazing interfacial structures between Cu and TiN sintered ceramics, which simulate the AlN–AMB interfacial structure, were analyzed in order to focus on the interfacial reaction between the Ag–Cu alloy layer and the TiN grain.

A solid-phase sintered ceramic without a grain boundary phase and a liquid-phase sintered ceramic with grain boundary phases such as a Ni-containing Fe phase and Mo_2C were used as the TiN sintered ceramics. No different phases were present on the TiN grain surfaces of these TiN sintered bonding surfaces.

No bonding was obtained between the TiN solid-phase sintered ceramic and the Ag–Cu alloy layer. Bonding of the Ag–Cu alloy layer and the TiN grains requires chemical bonding rather than mechanical bonding. In contrast, three types of interfacial structures were observed in the Cu/TiN liquid-phase sintered ceramic brazed specimen: Interface I (Cu-rich and Ag-rich phases/TiN grain brazing interface), Interface II (substituted Cu-rich and substituted Ag-rich phases/TiN grain interface), and Interface III (original grain boundary phases/TiN grain interface). These interfaces are characterized by the common feature that the TiN grains are bonded to the grain boundary phases through the Ni-containing Fe segregation layer

present before brazing in Interface III. This Ni-containing Fe segregation layer at Interface I is formed by the interfacial reaction between the TiN grains and the grain boundary phase components of the TiN liquid-phase sintered ceramic dissolved in the Ag–Cu liquid phase. In addition, a Cu-containing segregation layer is formed between the Ag-rich phase and the Ni-containing Fe segregation layer at both Interfaces I and II. The fundamental interfacial structure in this brazing system is as follows: Cu(Ag)-rich phase/Cu segregation layer/Fe- and Ni-containing layer/ TiN grain.

Declarations

References

1. Bresesti P, Kling WL, Hendriks RL, Vailati R (2007) HVDC connection of offshore wind farms to the transmission system. IEEE Trans Energy Convers 22:37–43
2. Kim CK, Sood VK, Jang GS, Lim SJ, Lee SJ (2009) HVDC Transmission: power conversion applications in power systems. Wiley, New York
3. Flourentzou N, Agelidis VG, Demetriades GD (2009) VSC-based HVDC power transmission systems: an overview. IEEE Trans Power Electron 24(3):592–602
4. Franck CM (2011) HVDC circuit breakers: a review identifying future research needs. IEEE Trans Power Deliv 26(2):998–1007
5. Echeverria J, Kouro S, Pérez M, Abu-rub H (2013) Multi-modular cascaded DC-DC converter for HVDC grid connection of large-scale photovoltaic power systems. In: Proceedings of IECON 2013, 39th annual conference of the IEEE industrial electronics society, pp 6999–7005
6. Burgess JF, Neugebauer CA, Flanagan G, Moore RE (1976) The direct bonding of metals to ceramics and application in electronics. Electrocompon Sci Technol 2:233–240
7. Iwase N, Anzai K, Shinozaki K (1986) Aluminum nitride substrates having high thermal conductivity. Solid State Technol 29(10):135–138
8. Schulz-Harder J (2003) Advantages and new development of direct bonded copper substrates. Microelectron Reliab 43(3):359–365
9. Carim AH, Loehman RE (1990) Microstructure at the interface between AlN and a Ag–Cu–Ti braze alloy. J Mater Res 5(7):1520–1529
10. Taranets NYu, Jones H (2004) Wettability of aluminium nitride based ceramics of different porosity by two active silver based brazing alloys. Mater Sci Eng, A 379:251–257
11. Terasaki N, Ohashi T, Nagatomo Y, Kuromitsu Y, Shirzadi AA (2019) A new method for liquid-phase bonding of copper plates to aluminum nitride (AlN) substrates used in high-power modules. J Mater Sci Mater Electron 30:6552–6555
12. Sivaprahasam D, Sujitha T, Gowtham U, Jayachandran B, Gopalan R (2021) Microstructure and heat transfer characteristics of active brazed ceramic–metal joints. Ceram Int 47:16133–16140
13. Zhang Y, Zhang J, Chen J (2021) Effect of interfacial microstructure evolution on the peeling strength and fracture of AMB Cu-metalized AlN substrate. J Am Ceram Soc 105:577–589
14. Piton M, Chauchat B, Servière JF (2018) Implementation of direct chip junction temperature measurement in high power IGBT module in operation-railway traction converter. Microelectron Reliab 88:1305–1310
15. Kato S, Yano T, Iseki T (1993) Interfacial structures between Ag–Cu–Ti alloys and sintered SiC with various additives. J Ceram Soc Jpn 101(3):325–330
16. Saitoh O, Suzumura A, Ogawa H (1996) The corrosion phenomena of ruby by active metal brazing filler (Ag–Cu–Ti) at the brazing interface. Q J Japan Weld Soc 14(4):717–722
17. Sun F-L, Feng J-C, Li D (2001) Bonding of CVD diamond thick films using an Ag–Cu–Ti brazing alloy. J Mater Process Technol 115(3):333–337
18. Loehman RE, Kotula PG (2004) Spectral imaging analysis of interfacial reactions and microstructures in brazing of alumina by a Hf–Ag–Cu alloy. J Am Ceram Soc 87(1):55–59
19. Ali M, Knowles KM, Mallinson PM, Fernie JA (2016) Interfacial reactions between sapphire and Ag–Cu–Ti-based active brazed alloys. Acta Mater 103:859–869
20. Simhan DR, Ghosh A (2018) Vacuum brazing of cubic boron nitride to medium carbon steel with Zr added passive and Ti activated eutectic Ag–Cu alloys. Ceram Int 44(5):4891–4899
21. Terasaki N, Sakaguchi M, Chiba H, Ohashi T, Nagatomo Y, Kuromitsu Y, Sekino T, Knowles KM (2022) Growth mechanism of TiN reaction layers produced on AlN via active metal bonding. J Mater Sci 57:13300–13313
22. Subrumanian PR, Perepezko JH (1993) The Ag–Cu (Silver-Copper) system. J Ph Equilibria 14(1):62–75
23. Kuzenkova MA, Kislyi PS (1971) Vacuum sintering of titanium nitride. Soviet Powder Metall Met Ceram 10:125–128
24. Owen EA, Sully AH (1941) On the migration of atoms in iron-nickel alloys. Lond, Edinb, Dublin Philos Mag J Sci 31(207):314–338
25. Ono K, Ueda Y, Yamaguchi A, Moriyama J (1977) Thermodynamic study of Fe–Ni solid solution. Trans Japan Inst Metals 18:610–616
26. Swartzendruber LJ, Itkin VP, Alcock CB (1991) The Fe–Ni (iron-nickel) system. J Ph Equilibria 12:288–312

27. EremenkoVelikanova VNTY (1965) The type of crystallization and composition of the higher molybdenum carbide. Soviet Powder Metall Met Ceram 4:30–32

28. Qin J, Huang Q, Wang X, Suo X, Wang J, Li H (2021) Interfacial metal/ceramic bonding mechanism for metallization of ceramics via cold spraying. J Mater Process Technol 288:116845